remote sensing

MDPI

Article

Doppler Spectrum-Based NRCS Estimation Method for Low-Scattering Areas in Ocean SAR Images

Hui Meng [1,2,3], Xiaoqing Wang [4,*], Jinsong Chong [1,2,*], Xiangfei Wei [1,2,3] and Weiya Kong [1,2,3]

1 National Key Laboratory of Science and Technology on Microwave Imaging, Beijing 100190, China; dream_kevin@126.com (H.M.); weixiangfei14@mails.ucas.ac.cn (X.W.); kongweiya13@mails.ucas.ac.cn (W.K.)
2 Institute of Electronics, Chinese Academy of Sciences, Beijing 100190, China
3 School of Electronics, Electrical and Communication Engineering, University of Chinese Academy of Sciences, Beijing 100190, China
4 Institute of Microelectronics of Chinese Academy of Sciences, Beijing 100029, China
* Correspondence: huadaqq@126.com (X.W.); iecas_chong@163.com (J.C.); Tel.: +86-10-8299-5990 (X.W.); +86-10-5888-7125 (J.C.)

Academic Editors: Xiaofeng Yang, Xiaofeng Li, Ferdinando Nunziata, Alexis Mouche and Prasad S. Thenkabail
Received: 6 December 2016; Accepted: 25 February 2017; Published: 28 February 2017

Abstract: The image intensities of low-backscattering areas in synthetic aperture radar (SAR) images are often seriously contaminated by the system noise floor and azimuthal ambiguity signal from adjacent high-backscattering areas. Hence, the image intensity of low-backscattering areas does not correctly reflect the backscattering intensity, which causes confusion in subsequent image processing or interpretation. In this paper, a method is proposed to estimate the normalized radar cross-section (NRCS) of low-backscattering area by utilizing the differences between noise, azimuthal ambiguity, and signal in the Doppler frequency domain of single-look SAR images; the aim is to eliminate the effect of system noise and azimuthal ambiguity. Analysis shows that, for a spaceborne SAR with a noise equivalent sigma zero (NESZ) of −25 dB and a single-look pixel of 8 m × 5 m, the NRCS-estimation precision of this method can reach −38 dB at a resolution of 96 m × 100 m. Three examples are given to validate the advantages of this method in estimating the low NRCS and the filtering of the azimuthal ambiguity.

Keywords: SAR; ocean; NRCS; Doppler spectrum; azimuthal ambiguity

1. Introduction

Areas with low normalized radar cross-section (NRCS) appear dark in synthetic aperture radar (SAR) images. It is frequently seen in ocean SAR images, such as those of oil spills, organic films, low wind areas, fronts, upwelling, current shear zones, and dark strips of internal waves and swells [1,2]. Among land targets, the backside of mountains and flat ground such as airport runways are also typical low-backscattering targets. The signal intensities of low-backscattering areas in SAR images are often close to or even less than the noise floor of the SAR system. Taking the ocean surface as an example; the mean NRCS of the ocean surface for the L, C, and X bands ranges from −15 dB to −25 dB at moderate wind speeds and incident angles. However, the NRCS of low-backscattering areas on the ocean surface is much lower than the mean NRCS of the ocean surface. The NRCS of low-backscattering areas of the ocean surface is often less than −30 dB, whereas the noise equivalent sigma zero (NESZ) of most spaceborne SAR systems ranges from −20 dB to −30 dB. Hence, the backscattering signal intensities of low-backscattering areas in ocean SAR images are often less than the noise floor of SAR systems. The NESZ values of typical spaceborne SAR systems are listed in Table 1 [3,4].

Table 1. Noise equivalent sigma zero (NESZ) values of typical spaceborne synthetic aperture radar (SAR) systems.

Satellite	Mode	NESZ (dB)
ERS-1/2		−21 to −24
Envisat	Image	−20 to −22
	Wave	−20 to −22
	Alternating Polarization	−19 to −22
	Wide Swath	−21 to −26
	Global Monitoring	−32 to −35
Radarsat-1		<−21
Radarsat-2	Standard	−31
	Fine	−28
	Wide	−23
	ScanSAR narrow	−23
	ScanSAR wide	−23
JERS-1		<−20.5
ALOS/PALSAR	Fine (Swath Width 70 km)	<−23
	Fine (Swath Width 60 km)	<−25
	Polarimetry	<−29
	ScanSAR	<−25
TerraSAR-X	Spotlight (HS)	−23
	Spotlight (LS)	−23
	Stripmap	−22
	ScanSAR	−21

Another factor that can affect the image intensities of low-backscattering areas is the azimuthal ambiguity effect of high-backscattering areas. It occurs because the Doppler frequency of the signal reflected from the area illuminated by the azimuthal sidelobe of the antenna exceeds the pulse repetition frequency (PRF). The azimuthal ambiguity signal of a target is located at a position with a certain displacement relative to its real position. This displacement depends on the PRF, the velocity of the platform and the Doppler centroid frequency of the SAR system. A typical value of the azimuthal ambiguity of a spaceborne SAR is about −15 dB to −20 dB. If the NRCS of a high-backscattering area is 15 dB to 20 dB higher than that of a low-backscattering area located at the position where the azimuthal ambiguity signal from the high-backscattering area is present, the azimuthal ambiguity signal could significantly affect the image intensity of the dark area. Azimuthal ambiguities are especially frequent in land–water junctions, because the NRCSs of land targets are much higher than that of the water surface.

Two analyses above indicate that, in order to estimate the certain value of the low areas' NRCS, the effect of the azimuthal ambiguity must be taken into consideration. Nevertheless, the standard radiometric calibration algorithm for SAR images only takes the system noise into account and ignores the azimuthal ambiguity effect, which is expressed in the following equation [5,6].

$$\sigma_{cal} = 10\lg(I - N_0) - K + 10\lg\left[\left(\frac{R}{R_{ref}}\right)^3 \frac{\sin\alpha}{\sin\alpha_{ref}} \frac{G_{ref}}{g(\alpha)G}\right] \quad (1)$$

where I, R, α, and G are the image intensity, slant range, elevation angle and system gain of a certain image pixel respectively; $g(\alpha)$ is the two-way antenna gain at elevation angle α, N_0 is the system noise, K is the calibration constant, and R_{ref}, α_{ref}, and G_{ref} are the slant range, elevation angle, and system gain of the reference target, respectively.

However, an accurate system noise N_0 is seldom provided in standard commercial spaceborne SAR data products. Moreover, even if a sufficiently accurate N_0 is provided, it is possible to obtain

a meaningless NRCS of less than or equal to zero because the image intensity is a stochastic variable that may be less than the system noise N_0, especially when the NRCS of the target is relatively low. Hence, in most practical NRCS calibration applications, the system noise is also ignored and Equation (1) is simplified as follows [5–10].

$$\sigma_{cal} = 10\lg(I) - K + 10\lg\left[\left(\frac{R}{R_{ref}}\right)^3 \frac{\sin\alpha}{\sin\alpha_{ref}} \frac{G_{ref}}{g(\alpha)G}\right] \quad (2)$$

When calibrated using Equation (2), the NRCS of low-backscattering areas inevitably includes a significant contribution from the system noise and azimuthal ambiguity, which can cause confusion in subsequent image processing and interpretation.

In this paper, a method of NRCS estimation for low-backscattering areas based on a spectrum is proposed. This method requires to know the noise floor N_0 and antenna patterns firstly. If N_0 and antenna patterns are unknown, we also can estimate them from a single-look complex SAR image. This method can also eliminate the azimuthal ambiguity effect according to the shape of the Doppler spectrum; avoiding a meaningless NRCS estimation by using the maximum likelihood (ML) estimation method and the modified Newton's iteration method.

The rest of this paper is organized as follows. Section 2 gives the details of the algorithms and principles used in this method. In Section 3, three examples are presented to validate the advantages of this method. In Section 4, an analysis of the estimation precision and simulations are stated. Finally, some conclusions are presented in Section 5.

2. Spectral-Based NRCS Estimation Method for Low-Scattering Areas in SAR Images

2.1. The Principle of the Proposed Method

2.1.1. Analysis of Doppler Spectrum Composition

From the SAR imaging theory [4–11], it is well known that the shape of system noise, azimuthal ambiguity, and the backscattering signal present different patterns in the Doppler spectrum of the SAR raw signal (here, it is supposed that the range match filtering and range cell migration correction have been done), i.e., the system noise power density is a certain constant in the Doppler spectrum, whereas the shape of the Doppler spectrum of the backscattering signal and azimuthal ambiguity depend on the antenna pattern: the backscattering signal and azimuthal ambiguity correspond to the main lobe and side lobe respectively. The Doppler spectrum of the SAR raw signal can be expressed as:

$$E[p_r(f, x_0, y_0)] = \sum_{n=-\infty}^{n=\infty} \overline{\sigma}(x_0 + nD_x, y_0 + nD_y) P_a(f - f_0 + nF_r) + \frac{N_0}{F_r} \quad (3)$$

In Equation (3) $\begin{bmatrix} x_0 & y_0 \end{bmatrix}$ are the center positions of the area where the Fourier transformation apply, and x_0 and y_0 are the coordinates in the flight and look directions, respectively, $E[\,]$ refers to the mathematic expectation, f denotes the Doppler frequency, and $p_r(f)$ denotes the azimuthal power spectrum of the SAR raw signal. $P_a(f)$ is the power spectrum function of an ideal point target with a 0 dB NRCS, the shape of which is determined by the two-way antenna azimuthal pattern. Further, f_0 is the Doppler centroid, F_r refers to the pulse repeat frequency of the SAR system, N_0 is the intrinsic noise floor of the SAR system, $\overline{\sigma}(x_0 - nD_x, y_0 - nD_y)$ is the mean NRCS of the pixels located between $\begin{bmatrix} x_0 - nD_x - L/2 & y_0 - nD_y \end{bmatrix}$ and $\begin{bmatrix} x_0 - nD_x + L/2 & y_0 - nD_y \end{bmatrix}$ (L is the data length for calculating the Doppler spectrum), D_x and D_y are the displacements in the flight and look

directions, respectively, between the position of the azimuthal ambiguity signal and the real target position. They can be written as:

$$D_x = \frac{R\lambda F_r}{2V},\ D_y = -\frac{\lambda^2 f_0 F_r R}{4V^2} \tag{4}$$

where R is the slant range of the target, λ is the radar wavelength, and V is the velocity of the SAR platform.

In Equation (3), $n = 0$ corresponds to the signal reflected from the mainlobe of the antenna, and $n \neq 0$ corresponds to the contribution from the azimuthal ambiguity effect. In general, among the azimuthal ambiguity signals, only $n = -1$ and 1, which correspond to the azimuthal ambiguity from the first azimuthal antenna sidelobes. Hence, Equation (3) can be simplified as:

$$\begin{aligned} E[p_r(f, x_0, y_0)] \approx{}& \overline{\sigma}(x_0, y_0) P_a(f - f_0) + \overline{\sigma}(x_0 + D_x, y_0 + D_y) P_a(f - f_0 + F_r) \\ &+ \overline{\sigma}(x_0 - D_x, y_0 - D_y) P_a(f - f_0 - F_r) + \frac{N_0}{F_r} \end{aligned} \tag{5}$$

Equation (5) indicates the shapes of the averaged power spectrum of the backscattering signal are determined by the antenna pattern $P_a(f)$ and N_0. To illustrate the shape difference of the power spectrum between system noise, azimuthal ambiguity, and the backscattering signal more clearly, a schematic diagram is given in Figure 1.

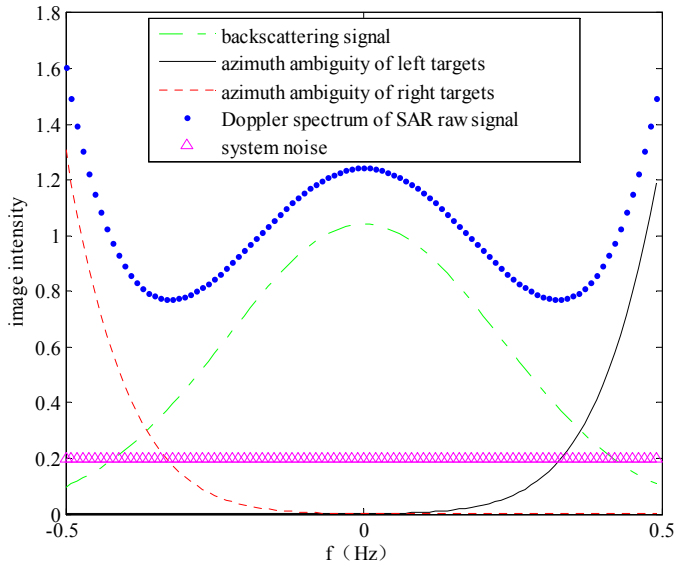

Figure 1. Schematic of the Doppler spectrum of synthetic aperture radar (SAR) raw signal and its various components.

Figure 1 is only a schematic diagram. When the image distribution is relatively uniform, the noise is the main disturbance. When there is a strong target around it, the azimuthal ambiguity is mainly from the strong target. From Figure 1, it is clear that the shapes of various components of the power spectrum of the SAR raw signal, composed of the backscattering signal, azimuthal ambiguity, and system noise, are very different. In general, the antenna pattern $P_a(f)$ and system noise N_0 can be acquired from the external and internal calibration of the SAR system. Therefore, it is possible to eliminate the effect of the azimuthal ambiguity on the NRCS estimation by taking full advantage of these differences. However, the azimuthal resolution of the SAR raw signal is too coarse for most applications. To increase the azimuthal resolution, the azimuthal matching filter must be applied on the SAR raw signal to convert it to a single-look complex image. However, the unweighted azimuthal matching filter can be used, which only changes the phase of the Doppler spectrum without modifying

the amplitude of the Doppler spectrum. Thus, the azimuthal power spectrum of the single-look complex image has the same shape characteristic with that of the SAR raw signal. The relation between the power spectra of single-look complex images and the SAR raw signal is given as:

$$p_s(f, x_0, y_0) = p_r(f, x_0, y_0)|H(f)|^2 = p_r(f, x_0, y_0) \tag{6}$$

where $H(f) = \exp\left(j\pi\frac{\lambda R f^2}{2V^2}\right)$ is the unweighted azimuthal matching filter, $p_s(f, x_0, y_0)$ and $p_r(f, x_0, y_0)$ are the azimuthal power spectra of the single-look complex image and the SAR raw signal, respectively.

The shape patterns shown in Figure 1 are the mathematics expectation of the power spectrum. The real power spectrum of a small patch of the single-look complex images is in fact a stochastic process. As the signal of a single-look complex image is a complex Gaussian process, the probability density function of each sample of the power spectrum can be given by the well-known exponential distribution that follows:

$$g(p_s(f, x_0, y_0)) = \frac{1}{E[p_s(f, x_0, y_0)]} \exp\left\{-\frac{p_s(f, x_0, y_0)}{E[p_s(f, x_0, y_0)]}\right\} \tag{7}$$

Equation (5) indicates that the backscattering signal $\overline{\sigma}(x_0, y_0)$ of a certain area contributes to three spectra: $p_s(f, x_0, y_0)$, $p_s(f, x_0 - D_x, y_0 - D_y)$, and $p_s(f, x_0 + D_x, y_0 + D_y)$. Hence, the joint condition probability density function of all the frequency points is:

$$\begin{aligned} &g\Big(\ p_s(f, x_0, y_0) \quad p_s(f, x_0 - D_x, y_0 - D_y) \quad p_s(f, x_0 + D_x, y_0 + D_y) \ \Big|\overline{\sigma}(x_0, y_0)\Big) \\ &= \prod_{i=1}^{m} \frac{1}{E[p_s(f_i, x_0, y_0)]} \exp\left\{-\frac{p_s(f_i, x_0, y_0)}{E[p_s(f_i, x_0, y_0)]}\right\} \\ &\prod_{i=1}^{m} \frac{1}{E\left[p_s(f_i, x_0 - D_x, y_0 - D_y)\right]} \exp\left\{-\frac{p_s(f_i, x_0 - D_x, y_0 - D_y)}{E\left[p_s(f_i, x_0 - D_x, y_0 - D_y)\right]}\right\} \\ &\prod_{i=1}^{m} \frac{1}{E\left[p_s(f_i, x_0 + D_x, y_0 + D_y)\right]} \exp\left\{-\frac{p_s(f_i, x_0 + D_x, y_0 + D_y)}{E\left[p_s(f_i, x_0 + D_x, y_0 + D_y)\right]}\right\} \end{aligned} \tag{8}$$

where m is the point number of the discrete Doppler spectrum.

Moreover, the image intensity is also a stochastic process related to the backscattering signal. In general, if the image pitch is small enough, the probability density function of a multi-look image intensity of an image pitch can be modeled by a gamma distribution as follows:

$$g_p(I(x_0, y_0)) = \begin{cases} \dfrac{M^M I^{M-1}(x_0, y_0)}{\left[E_c\overline{\sigma}(x_0, y_0) + E_l\overline{\sigma}(x_0 - D_x, y_0 - D_y) + E_R\overline{\sigma}(x_0 + D_x, y_0 + D_y)\right]^L \Gamma(M)} \\ \exp\left(-\dfrac{MI(x_0, y_0)}{E_c\overline{\sigma}(x_0, y_0) + E_l\overline{\sigma}(x_0 - D_x, y_0 - D_y) + E_R\overline{\sigma}(x_0 + D_x, y_0 + D_y)}\right) & I(x_0, y_0) > 0 \\ 0 & I(x_0, y_0) \le 0 \end{cases} \tag{9}$$

where M is the look number, $I(x_0, y_0)$ is the mean image intensity of a certain area with the center located at $[x_0, y_0]$. E_c, E_l, and E_R are the main lobe, left side lobe, and right side lobe factors, respectively:

$$E_c = \int_{-F_r/2}^{F_r/2} P_a(f - f_0)df,\ E_l = \int_{-F_r/2}^{F_r/2} P_a(f - f_0 - F_r)df,\ E_r = \int_{-F_r/2}^{F_r/2} P_a(f - f_0 + F_r)df \tag{10}$$

To estimate higher resolution NRCS from the power spectrum, the single-look complex images are divided into many small pitches and the Fourier transformation is applied on each image patch.

After obtaining $P_a(f)$ and N_0, the local NRCS can be further estimated from the Doppler spectrum. In this step, L is selected according to the desired final resolution, but it cannot be significantly larger.

2.1.2. Methods and Solutions to Estimate the NRCS from the Doppler Spectrum

Suppose that a SAR single-look complex image has been corrected. For example, the range shift caused by the azimuthal ambiguity has been compensated, and the image has been interpolated k times in azimuth. Meanwhile, the azimuthal shift caused by the azimuthal ambiguity is X times larger than emphL. The corrected image is divided into some small patches. The size of every patch is about $R_m \times R_a$ (range multiplied by azimuthal). Choosing a row of azimuthal patches, and supposing that the scattering coefficient of every patch is $\sigma_1, \sigma_2, \ldots, \sigma_T$, respectively, the Doppler spectrum of the i-th block is f_{i_m}.

Estimating NRCS from Doppler spectrum is a typical Bayesian estimation problem [12,13], which is expressed as the following equation.

$$\begin{aligned}\hat{\sigma}_i = \underset{\overline{\sigma}(x_0,y_0)}{\operatorname{argmax}}[g\,(p(f_{i\_1}), p(f_{i\_2}), ..., p(f_{i\_m}), p(f_{i-\mathrm{X}\_1}), p(f_{i-\mathrm{X}\_2}), ..., \\ p(f_{i-\mathrm{X}\_m}), p(f_{i+\mathrm{X}\_1}), p(f_{i+\mathrm{X}\_2}), ..., p(f_{i+\mathrm{X}\_m})|\overline{\sigma}_i) g_p(\overline{\sigma}(x_0,y_0))]\end{aligned} \tag{11}$$

The estimation equation of single patches can be expressed as:

$$\hat{\sigma}(x_0,y_0) = \underset{\overline{\sigma}(x_0,y_0)}{\operatorname{argmax}}\left[g(p(f_1), p(f_2), ..., p(f_m)|\overline{\sigma}(x_0,y_0)) g_p(\overline{\sigma}(x_0,y_0))\right] \tag{12}$$

where $\hat{\sigma}(x_0,y_0)$ is the estimation of $\overline{\sigma}(x_0,y_0)$, f_i $(i = 1,2,...m)$ is the discrete frequency point, m is the point number of the discrete Doppler spectrum, $g(p(f_1), p(f_2), ..., p(f_m)|\overline{\sigma}(x_0,y_0))$ refers to the conditional probability density function of the Doppler spectrum, and $g_p(\overline{\sigma}(x_0,y_0))$ refers to the a-priori probability density of $\overline{\sigma}(x_0,y_0)$.

Bayesian estimation is a global optimal estimation method. It increases the estimation precision at the NRCS with high a-priori probability density, but decreases the estimation precision at the NRCS with low a-priori probability density. In general, the a-priori probability density of the NRCS of a SAR image can be expressed by models such as Gamma, inverse Gaussian, or other distribution models [14]. However, in these commonly used models, the probability densities of low-NRCS are relatively low, which will lead to a less accurate estimation result for the low-backscattering areas. Hence, to acquire a higher estimation precision for the low-backscattering areas, the commonly used NRCS distribution models are not adopted, but it is assumed that the a-priori probability density of the NRCS is uniformly distributed. Another point which should be considered is that the NRCS should be greater than zero. Therefore, the a-priori probability density of the NRCS used in this paper is given as:

$$g_p(\sigma) = \begin{cases} 1 & \sigma > 0 \\ 0 & \sigma \leq 0 \end{cases} \tag{13}$$

The Equation (13) is used as the new a-priori probability density in proposed method, then the NRCS is estimated by the maximum likelihood (ML) estimation method. The advantage of the proposed method is that it can avoid meaningless estimation results less than or equal to zero.

Because the a-priori probability density given by Equation (13) is a discontinuous function, which is not convenient for the solving of Equation (11), it is approximated by:

$$g_p(\sigma) = \frac{1}{2} + \frac{1}{\pi}\arctan(\alpha\sigma) \tag{14}$$

where, in order to match Equation (13), α should be more than 10^{16} and choose 10^{20} in this method.

The estimation of Equation (12) can be obtained by solving the following equation:

$$\begin{aligned}&\frac{\partial \ln g\left(\begin{array}{cccc} p_n(f_1) & p_n(f_2) & \cdots & p_n(f_m) \end{array}\middle|\overline{\sigma}_n\right)}{\partial\overline{\sigma}_n}+\frac{\partial \ln g\left(\begin{array}{cccc} p_{n-X}(f_1) & p_n(f_2) & \cdots & p_n(f_m) \end{array}\middle|\overline{\sigma}_n\right)}{\partial\overline{\sigma}_n}\\&+\frac{\partial \ln g\left(\begin{array}{cccc} p_{n+X}(f_1) & p_{n+X}(f_2) & \cdots & p_{n+X}(f_m) \end{array}\middle|\overline{\sigma}_n\right)}{\partial\overline{\sigma}_n}+\frac{\partial \ln g_p(\overline{\sigma}_n|)}{\partial\overline{\sigma}_n}=0\end{aligned} \tag{15}$$

where $p_n(f_i)$ is the i-th frequency of the n-th block.

Because the signal of a single-look complex image is a complex Gaussian process, the probability density function of each sample of the Doppler spectrum can be given by the well-known exponential distribution as follows:

$$g(\,p(f)|\overline{\sigma}(x_0,y_0))=\frac{1}{E[p(f)]}\exp\left\{-\frac{p(f)}{E[p(f)]}\right\} \tag{16}$$

Thus, the joint probability density function of all the frequency points is:

$$g(p(f_1)p(f_2)\cdots p(f_m)|\overline{\sigma}(x_0,y_0))=\prod_{i=1}^{m}\frac{1}{E[p(f_i)]}\exp\left\{-\frac{p(f_i)}{E[p(f_i)]}\right\} \tag{17}$$

Inserting Equations (5), (16) and (17) into Equation (15), and considering that the Doppler spectrum at different azimuthal locations has different components, thus, the following functions at different azimuthal locations are derived.

When $2X < n \leq \mathrm{T} - 2X$

$$\begin{aligned}&-\sum_{i=1}^{m}\frac{P_C(f_i)}{\left[\overline{\sigma}_{n-X}P_L(f_i)+\overline{\sigma}_nP_C(f_i)+\overline{\sigma}_{n+X}P_R(f_i)+\frac{N_0}{F_r}\right]}-\sum_{i=1}^{m}\frac{P_R(f_i)}{\left[\overline{\sigma}_{n-2X}P_L(f_i)+\overline{\sigma}_{n-X}P_C(f_i)+\overline{\sigma}_nP_R(f_i)+\frac{N_0}{F_r}\right]}\\&-\sum_{i=1}^{m}\frac{P_L(f_i)}{\left[\overline{\sigma}_nP_L(f_i)+\overline{\sigma}_{n+X}P_C(f_i)+\overline{\sigma}_{n+2X}P_R(f_i)+\frac{N_0}{F_r}\right]}+\sum_{i=1}^{m}\frac{p_n(f_i)P_C(f_i)}{\left[\overline{\sigma}_{n-X}P_L(f_i)+\overline{\sigma}_nP_C(f_i)+\overline{\sigma}_{n+X}P_R(f_i)+\frac{N_0}{F_r}\right]^2}\\&+\sum_{i=1}^{m}\frac{p_{n-X}(f_i)P_R(f_i)}{\left[\overline{\sigma}_{n-2X}P_L(f_i)+\overline{\sigma}_{n-X}P_C(f_i)+\overline{\sigma}_nP_R(f_i)+\frac{N_0}{F_r}\right]^2}+\sum_{i=1}^{m}\frac{p_{n+X}(f_i)P_L(f_i)}{\left[\overline{\sigma}_nP_L(f_i)+\overline{\sigma}_{n+X}P_C(f_i)+\overline{\sigma}_{n+2X}P_R(f_i)+\frac{N_0}{F_r}\right]^2}\\&+\frac{\alpha}{[1+(\alpha\overline{\sigma}_n)][\frac{\pi}{2}+\arctan(\alpha\overline{\sigma}_n)]}=0\end{aligned} \tag{18}$$

where $P_C(f_i) = P_a(f_i - f_0)$, $P_L(f_i) = P_a(f_i - f_0 - F_r)$, and $P_R(f_i) = P_a(f_i - f_0 + F_r)$; n refers to the pixel location in the flight directions. T is the length of the azimuthal data. X is the number of the azimuthal ambiguity.

When $X < n \leq 2X$:

$$\begin{aligned}&-\sum_{i=1}^{m}\frac{P_C(f_i)}{\left[\overline{\sigma}_{n-X}P_L(f_i)+\overline{\sigma}_nP_C(f_i)+\overline{\sigma}_{n+X}P_R(f_i)+\frac{N_0}{F_r}\right]}-\sum_{i=1}^{m}\frac{P_L(f_i)}{\left[\overline{\sigma}_nP_L(f_i)+\overline{\sigma}_{n+X}P_C(f_i)+\overline{\sigma}_{n+2X}P_R(f_i)+\frac{N_0}{F_r}\right]}\\&+\sum_{i=1}^{m}\frac{p_n(f_i)P_C(f_i)}{\left[\overline{\sigma}_{n-X}P_L(f_i)+\overline{\sigma}_nP_C(f_i)+\overline{\sigma}_{n+X}P_R(f_i)+\frac{N_0}{F_r}\right]^2}+\sum_{i=1}^{m}\frac{p_{n+X}(f_i)P_L(f_i)}{\left[\overline{\sigma}_nP_L(f_i)+\overline{\sigma}_{n+X}P_C(f_i)+\overline{\sigma}_{n+2X}P_R(f_i)+\frac{N_0}{F_r}\right]^2}\\&+\frac{\alpha}{[1+(\alpha\overline{\sigma}_n)][\frac{\pi}{2}+\arctan(\alpha\overline{\sigma}_n)]}=0\end{aligned} \tag{19}$$

When $0 < n \leq X$:

$$-\sum_{i=1}^{m}\frac{P_L(f_i)}{\left[\overline{\sigma}_n P_L(f_i)+\overline{\sigma}_{n+X}P_C(f_i)+\overline{\sigma}_{n+2X}P_R(f_i)+\frac{N_0}{F_r}\right]}+\sum_{i=1}^{m}\frac{p_{n+X}(f_i)P_L(f_i)}{\left[\overline{\sigma}_n P_L(f_i)+\overline{\sigma}_{n+X}P_C(f_i)+\overline{\sigma}_{n+2X}P_R(f_i)+\frac{N_0}{F_r}\right]^2}$$
$$+\frac{\alpha}{[1+(\alpha\overline{\sigma}_n)][\frac{\pi}{2}+\arctan(\alpha\overline{\sigma}_n)]}=0 \quad (20)$$

When $\mathrm{T}-2X < n \leq \mathrm{T}-X$:

$$-\sum_{i=1}^{m}\frac{P_C(f_i)}{\left[\overline{\sigma}_{n-X}P_L(f_i)+\overline{\sigma}_n P_C(f_i)+\overline{\sigma}_{n+X}P_R(f_i)+\frac{N_0}{F_r}\right]}-\sum_{i=1}^{m}\frac{P_R(f_i)}{\left[\overline{\sigma}_{n-2X}P_L(f_i)+\overline{\sigma}_{n-X}P_C(f_i)+\overline{\sigma}_n P_R(f_i)+\frac{N_0}{F_r}\right]}$$
$$+\sum_{i=1}^{m}\frac{p_n(f_i)P_C(f_i)}{\left[\overline{\sigma}_{n-X}P_L(f_i)+\overline{\sigma}_n P_C(f_i)+\overline{\sigma}_{n+X}P_R(f_i)+\frac{N_0}{F_r}\right]^2}+\sum_{i=1}^{m}\frac{p_{n-X}(f_i)P_R(f_i)}{\left[\overline{\sigma}_{n-2X}P_L(f_i)+\overline{\sigma}_{n-X}P_C(f_i)+\overline{\sigma}_n P_R(f_i)+\frac{N_0}{F_r}\right]^2} \quad (21)$$
$$+\frac{\alpha}{[1+(\alpha\overline{\sigma}_n)][\frac{\pi}{2}+\arctan(\alpha\overline{\sigma}_n)]}=0$$

When $\mathrm{T}-X < n \leq \mathrm{T}$:

$$-\sum_{i=1}^{m}\frac{P_R(f_i)}{\left[\overline{\sigma}_{n-2X}P_L(f_i)+\overline{\sigma}_{n-X}P_C(f_i)+\overline{\sigma}_n P_R(f_i)+\frac{N_0}{F_r}\right]}+\sum_{i=1}^{m}\frac{p_{n-X}(f_i)P_R(f_i)}{\left[\overline{\sigma}_{n-2X}P_L(f_i)+\overline{\sigma}_{n-X}P_C(f_i)+\overline{\sigma}_n P_R(f_i)+\frac{N_0}{F_r}\right]^2} \quad (22)$$
$$+\frac{\alpha}{[1+(\alpha\overline{\sigma}_n)][\frac{\pi}{2}+\arctan(\alpha\overline{\sigma}_n)]}=0$$

Combining all the equations above, there are n equations. To solve all the unknown variables, the Newton iterative method is adopted. The Jacobian matrix of the derived function is in the Appendix A.

To solve $\overline{\sigma}(x_0, y_0)$ from all equations above, $\overline{\sigma}(x_0 - D_x, y_0 - D_y)$ and $\overline{\sigma}(x_0 + D_x, y_0 + D_y)$ should be first known. However, to obtain $\overline{\sigma}(x_0 - D_x, y_0 - D_y)$ or $\overline{\sigma}(x_0 + D_x, y_0 + D_y)$, a known $\overline{\sigma}(x_0, y_0)$ is also needed. This self-contradiction problem can be addressed by using an iterative strategy. In the n-th iteration, Equation (17) is written as:

$$\sum_{i=1}^{m}\frac{P_a(f_i-f_0)}{\left[\overline{\sigma}_n(x_0,y_0)P_a(f-f_0)+\overline{\sigma}_{n-1}(x_0+D_x,y_0+D_y)P_a(f-f_0+F_r)+\overline{\sigma}_{n-1}(x_0-D_x,y_0-D_y)P_a(f-f_0-F_r)+\frac{N_0}{F_r}\right]}$$
$$=\sum_{i=1}^{m}\frac{p(f_i)P_a(f_i-f_0)}{\left[\overline{\sigma}_n(x_0,y_0)P_a(f-f_0)+\overline{\sigma}_{n-1}(x_0+D_x,y_0+D_y)P_a(f-f_0+F_r)+\overline{\sigma}_{n-1}(x_0-D_x,y_0-D_y)P_a(f-f_0-F_r)+\frac{N_0}{F_r}\right]^2} \quad (23)$$
$$+\frac{\alpha}{[1+(\alpha\overline{\sigma}_n)][\frac{\pi}{2}+\arctan(\alpha\overline{\sigma}_n)]}$$

where $\overline{\sigma}_n(x_0, y_0)$ is the estimation result in the n-th iteration. The initial guess of $\overline{\sigma}(x_0, y_0)$ is given as:

$$\overline{\sigma}_0(x_0,y_0)=\begin{cases}\dfrac{\overline{I}(x_0,y_0)-\overline{I}(x_0+D_x,y_0+D_y)A-\overline{I}(x_0-D_x,y_0-D_y)A}{1-2A}-N_0 \\ ,\overline{I}(x_0,y_0)>\overline{I}(x_0+D_x,y_0+D_y)A+\overline{I}(x_0-D_x,y_0-D_y)A+(1-2A)N_0 \\ \sigma_{\min}, \\ ,\overline{I}(x_0,y_0)\leq\overline{I}(x_0+D_x,y_0+D_y)A+\overline{I}(x_0-D_x,y_0-D_y)A+(1-2A)N_0\end{cases} \quad (24)$$

where $\overline{I}(x_0, y_0)$ is the mean image intensity of the pixels between $\begin{bmatrix} x_0 - L/2 & y_0 \end{bmatrix}$ and $\begin{bmatrix} x_0 + L/2 & y_0 \end{bmatrix}$, A is the azimuthal ambiguity factor which is given by:

$$A=\int_{-F_r/2}^{-3F_r/2}P_a(\mathrm{f})\mathrm{df} \quad (25)$$

The convergence condition is given by:

$$\frac{\sum_{y_0}\sum_{x_0}|\overline{\sigma}_n(x_0,y_0)-\overline{\sigma}_{n-1}(x_0,y_0)|}{N_xN_y}<\sigma_{\min} \tag{26}$$

where $\sigma_{\min}$ refers to a certain small NRCS value. N_x and N_y are the pixel numbers of the estimated NRCS image in flight and look directions, respectively.

The aforementioned $\overline{\sigma}(x_0,y_0)$ is a relative backscattering intensity rather than an absolute NRCS. If we have the *K*-constant needed in the radiometric calibration, the estimated relative backscattering intensity $\overline{\sigma}(x_0,y_0)$ can be further converted to the absolute NRCS by replacing $I-N_0$ in Equation (1) with $\overline{\sigma}(x_0,y_0)$ estimated by this method, expressed as:

$$\sigma_{cal}(x_0,y_0)=10\lg[\overline{\sigma}(x_0,y_0)]-K+10\lg\left[\left(\frac{R}{R_{ref}}\right)^3\frac{\sin\alpha}{\sin\alpha_{ref}}\frac{G_{ref}}{g(\alpha)G}\right] \tag{27}$$

2.2. Algorithm Flow Chart and Summary

The azimuthal matching filters of the standard imaging algorithm of commercial SAR products are generally weighted filters, which does not satisfy the requirements of our method. Thus, our algorithm begins with the SAR raw data product. In the first step, SAR imaging, an unweighted azimuthal matching filter is used. The byproduct of SAR imaging is the Doppler centroids of each range cell, which will be used in the second step. The method shifts the Doppler centroids of the single-look complex images to a zero frequency position. This includes some substeps, such as fast Fourier transform (FFT), inverse FFT, and spectrum shifting. In the last step, the single-look complex image is divided into many subimage patches first. The size of the subimage patches is selected based on the desired resolution. Then, an iteration strategy is used to estimate the signal intensities of each subimage patch. In each iteration, the signal intensities are estimated on the basis of Equation (23), which is solved by the Newton-iteration algorithm. Finally, the estimated relative backscattering intensity $\overline{\sigma}(x_0,y_0)$ is converted to absolute NRCS using Equation (27).

The algorithm used in this method is summarized in Figure 2.

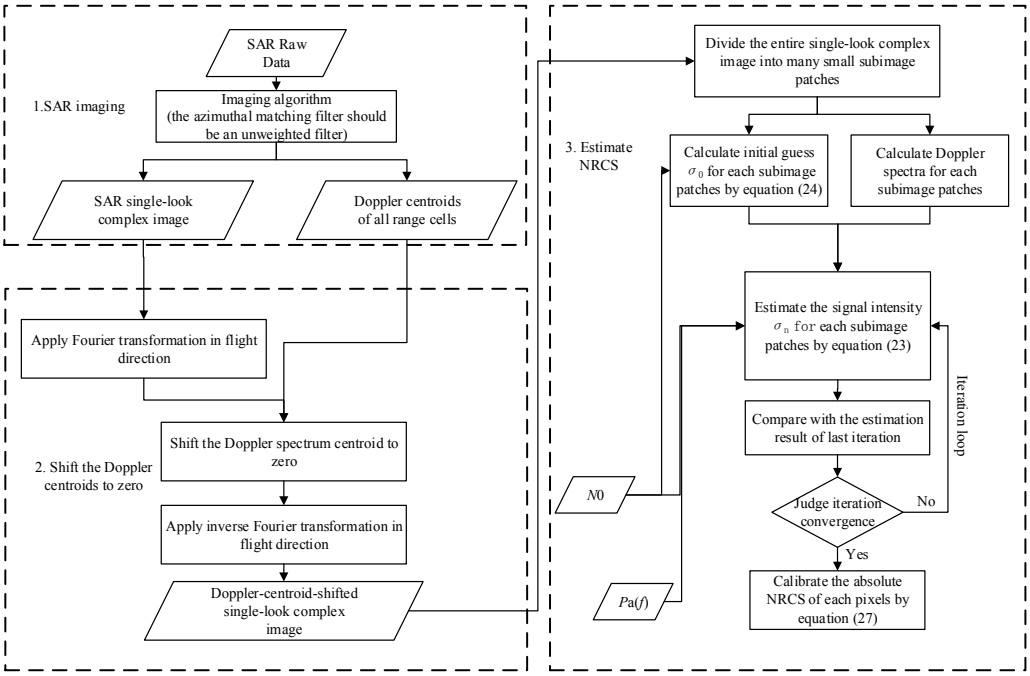

Figure 2. Algorithm flow chart.

3. Validation of the Proposed Estimation Method

In this section, three examples will be presented to demonstrate the advantages of this method in low NRCS estimation and azimuthal ambiguity filtering.

3.1. Example 1: Qualitative Analysis for the Estimation Method in Low NRCS

The first example is an ocean image acquired by ERS-2 (European remote sensing satellite (ERS) was the European Space Agency's first Earth-observing satellite) on 30 April 2005 in the South China Sea as a qualitative analysis, which is shown in Figure 3. There are 4912 pixels in the look direction and 28,695 pixels in the flight direction in the single-look complex image used in this example. Frame 1 in Figure 3 is a subimage for the comparison between a conventional SAR image and the corresponding estimated NRCS image.

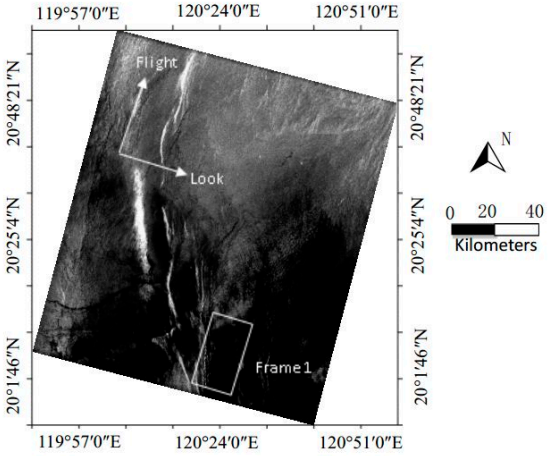

Figure 3. ERS-2 (European remote sensing satellite (ERS) was the European Space Agency's first Earth-observing satellite) ocean SAR image of South China Sea collected on 30 April 2005, at 02:28 UTC. Frame 1 is a subimage for the comparison between conventional SAR image and the corresponding estimated NRCS image.

The first step is estimating the Doppler centroid f_0 for each range cell [11,15–19], and then shifting the Doppler spectrum centroid of the single-look complex image to zero. Note that ocean currents can lead to an additional local shift of the Doppler centroid [20–22]. However, the Doppler shift resulting from the ocean current is generally less than 5% of the PRF, which can be neglected in the method proposed in this paper. Examples of unshifted and shifted Doppler spectra are shown in Figure 4.

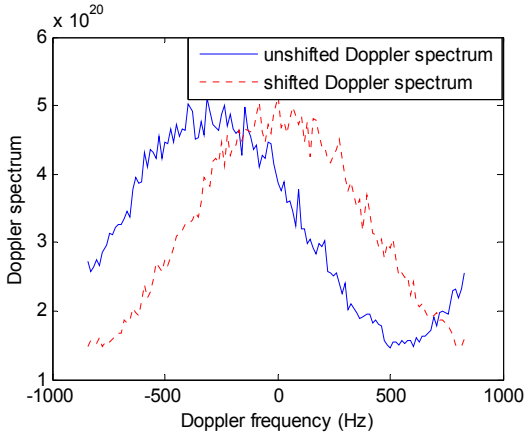

Figure 4. Unshifted and shifted Doppler spectra.

The second step is calculating Doppler spectra from the single-look complex image. In this example, each Doppler spectrum is a 128-point discrete spectrum that is averaged by 224 times in the flight direction and 10 times in the look direction. A total of 491 Doppler spectra from the entire SAR image are obtained. The azimuthal length used for calculating one Doppler spectrum is about 121 km (i.e., L = 121 km).

Frame 1 in Figure 3 is chosen to compare the conventional SAR image with the corresponding estimated NRCS image. The result is shown in Figure 5. The pixel size of the single-look complex image is about 21 m (range direction) × 4.2 m (flight direction). Figure 5a is a multi-look SAR image, in which each pixel is averaged by 80 adjacent pixels of the single-look complex image (4 pixels in the look direction × 20 pixels in the flight direction). Figure 5b is the estimated NRCS image, in which each pixel is estimated from 80 pixels of the single-look complex image (in each estimation, the Doppler spectrum is calculated from 20 pixels in the flight direction and averaged by 4 times in the look direction). The pixel sizes of both images in Figure 5 are about 84 m × 84 m. The image intensities of both images are shown by logarithmic grayscaling to display clear texture features of the dark area.

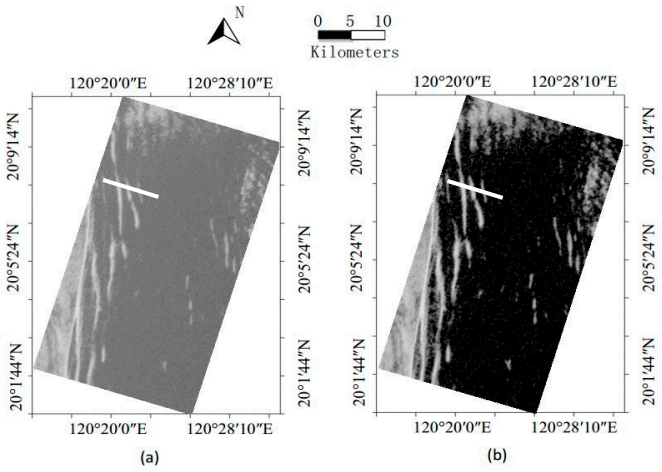

Figure 5. Subimages of Frame 1 in Figure 3, (**a**) conventional SAR image; (**b**) estimated normalized radar cross-section (NRCS) image.

The comparison of Figure 5a,b demonstrates that Figure 5b presents the features of the dark area more clearly. To compare these two images qualitatively, the image intensity profiles along the white lines are depicted in Figure 6.

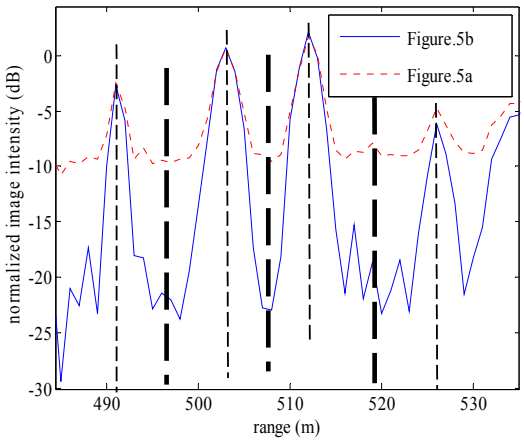

Figure 6. Image intensities along the white lines in Figure 5a (red dotted line) and Figure 5b (blue solid line).

In Figure 6, the signal intensity is normalized by the mean intensity of the entire image. The image feature near the white line is an oceanic internal wave. Four peaks of the internal wave are marked by dashed lines, and three troughs are marked by bold dashed lines. At the positions of the peaks, the estimated NRCS intensity is very close to that of conventional SAR image intensity because the SNR of the peaks is sufficiently high. As a comparison, at the positions of the troughs, the SAR signal is buried by the noise floor (about −10 dB after normalization), making it hard to judge the exact trough position. In contrast, the estimated NRCS can remove the effect of the noise floor to a large extent, and the trough positions of the estimated NRCS are near the midpoint of the two adjacent peaks, which indirectly validates the correctness of the proposed method.

3.2. Example 2: Quantitative Analysis for the Estimation Method in Low NRCS

This example is the atmospheric gravity waves' image acquired by ERS-2 on 11 March 2006 in the East China Sea as a quantitative analysis, which is shown in Figure 7. There are 4912 pixels in the look direction and 28,695 pixels in the flight direction in the single-look complex image used in this example.

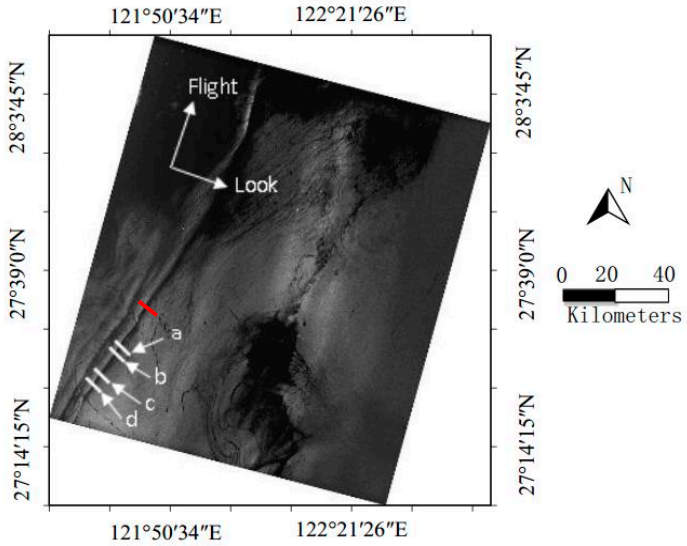

Figure 7. ERS-2 Ocean SAR image of the East China Sea collected on 11 March 2006, at 02:24 UTC. The four white data lines a, b, c, and d are the profiles for comparison between the proposed method, the SAR raw image intensity minus N_0 and the optimal parameter estimation method of internal waves [23].

In this example, the method of optimal parameter estimation of internal waves in SAR images [23] and the proposed method in this paper will be used to deal with the internal wave in Figure 7.

The optimal parameter estimation is the latest method for estimating the parameter of internal solitary waves. In this article, it is referred to as optimal parameter estimation. In order to verify the feasibility of this method, we found a section at the other location of atmospheric gravity waves (the red solid line region in Figure 7. The estimation result is shown in Figure 8, showing that the optimum estimators are very close to the Cramér–Rao bound (CRB). Therefore, the estimation method in the literature [23] is considered to fit the atmospheric gravity waves' profile in Figure 7.

We selected four profiles from the atmospheric gravity waves in Figure 7, and at the position of the trough, the SAR signal is buried by the noise floor at positions a and b are more obvious than positions c and d. The estimation method in the literature [23], the proposed method and the SAR Raw Image are used in the four profiles for comparison, The results of the comparison are shown in Figure 9.

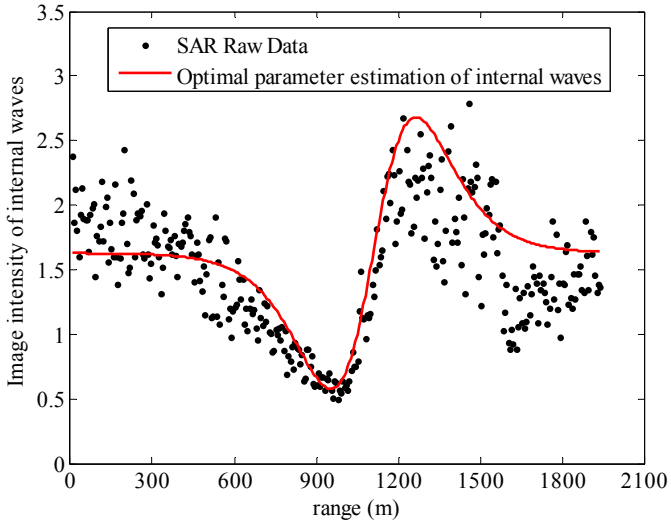

Figure 8. The validation of the optimal parameter estimation of internal waves.

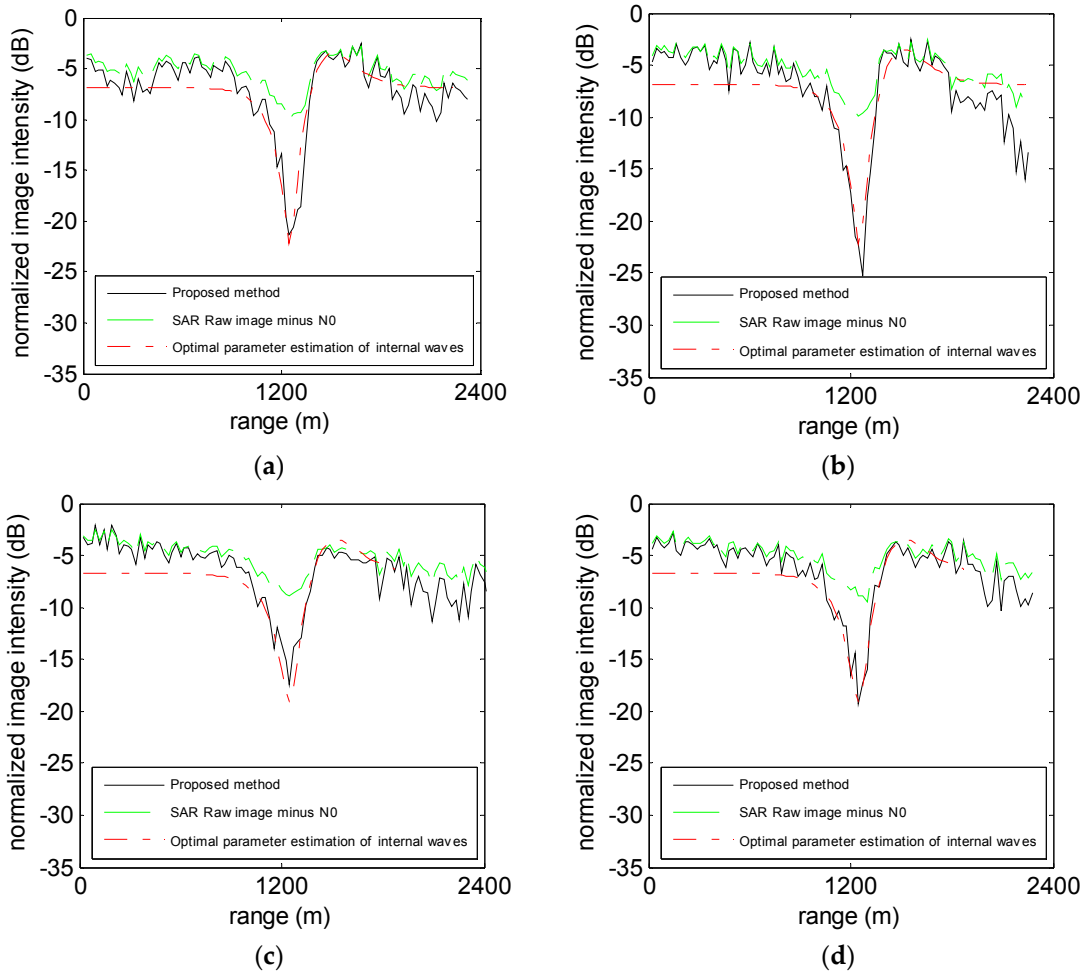

Figure 9. Image intensities along the four white lines in Figure 7. (**a**) the profile a in Figure 7; (**b**) the profile b in Figure 7; (**c**) the profile c in Figure 7; (**d**) the profile d in Figure 7; The green dashed line is the SAR raw image intensity minus N_0; the black solid line is the proposed method in this paper; the red dot dash line is the optimal parameter estimation method of internal waves.

In Figure 9, the signal intensity is normalized by the mean intensity of the entire image. The image feature near the white lines represent atmospheric gravity waves. At the position of the peak, the estimated NRCS intensity of all the profiles are very close to that of conventional SAR image intensity due to sufficiently high SNR of the peak. As a comparison, at the position of the trough, the SAR signal is buried by the noise floor (about −10 dB after normalization at positions a and b, and about −5 dB to −8 dB at positions c and d), making it hard to judge the exact trough position. In contrast, the estimated NRCS can remove the effect of the noise floor, which can reach −22 dB after normalization at positions a and b, and about −16 dB to −18 dB at positions of c and d. Position a is selected as an example through the method of optimal Parameter Estimation of Internal Waves in SAR images from the literature [23] to estimate the energy intensity value in the wave trough position, which is around −22 dB. From Figure 9, the estimation curve of signal intensity by the proposed method in this paper is very close to the method of optimal Parameter Estimation of Internal Waves in SAR images, which directly validates the accuracy of the proposed method.

3.3. Example 3: Validation of the Azimuthal Ambiguity Analysis

The third example is a RADARSAT-1 (RADARSAT is a Canadian remote sensing Earth observation satellite program overseen by the Canadian Space Agency) image of Vancouver, which is shown in Figure 10. The SAR raw data of this example was obtained from the accompanying CD of literature [11].

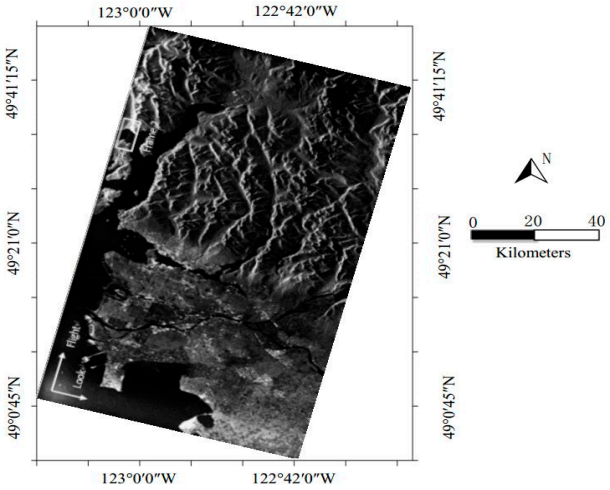

Figure 10. RADARSAT-1 (RADARSAT is a Canadian remote sensing Earth observation satellite program overseen by the Canadian Space Agency) SAR image of Vancouver collected on 16 June 2002, at 02:24 UTC.

There are 7940 pixels in the look direction and 19,425 pixels in the flight direction in the single-look complex image of this example. As in the first example, each Doppler spectrum in this example is also a 128-point discrete spectrum, which is averaged by 151 times in the flight direction and 30 times in the look direction. A total of 264 Doppler spectra can be obtained from the entire single-look complex image. The azimuthal length used for calculating one Doppler spectrum is about 109 km (i.e., L = 109 km).

Using Frame 2 in Figure 10 as an example, the conventional SAR image and the corresponding estimated NRCS image are shown in Figure 11. The pixel size of the single-look complex image is about 8 m (look direction) × 5.6 m (flight direction). Figure 11a is a multi-look SAR image, in which each pixel is averaged by 192 adjacent pixels of the single-look complex image (12 pixels in the look direction × 16 pixels in the flight direction). Figure 11b is an estimated NRCS image, in which each pixel is estimated from 192 pixels of the single-look complex image (in each estimation, the Doppler spectrum is calculated from 16 pixels in the flight direction and averaged by 12 times in the look direction). The pixel sizes of both images are about 96 m × 90 m.

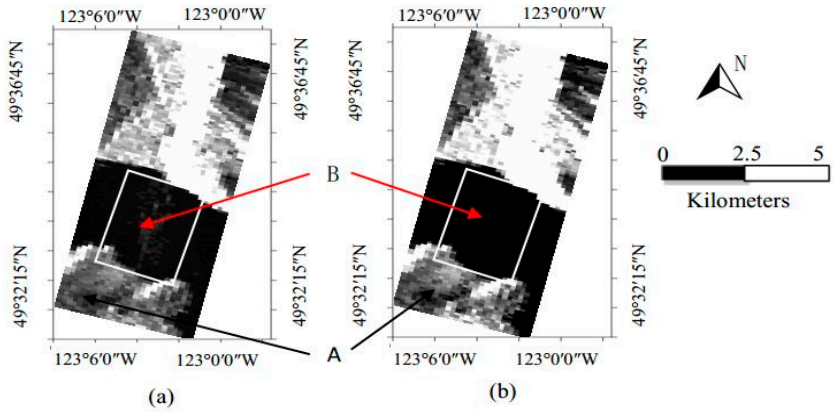

Figure 11. Subimage of Frame 2 in Figure 10, (**a**) conventional SAR image; (**b**) estimated NRCS image.

The white frame in Figure 11a is contaminated by the azimuthal ambiguity signal from the strong land targets to the right. As a comparison, the azimuthal ambiguity signal is filtered quite clearly in the same position in Figure 11b.

Points A and B in Figure 11a are selected to illuminate the difference in the Doppler spectrum between the signals contaminated and uncontaminated by the azimuthal ambiguity. The Doppler spectra of points A and B are shown in Figure 12.

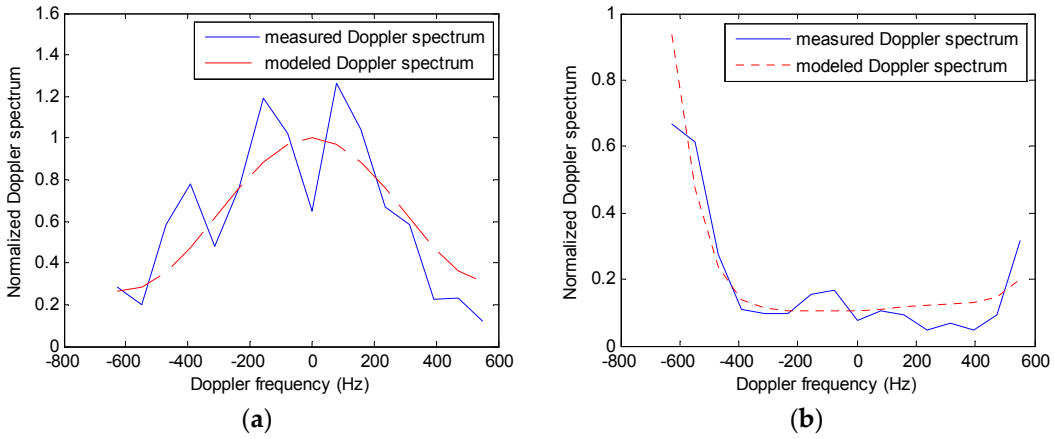

Figure 12. (**a**) Doppler spectrum of point A in Figure 11a; (**b**) Doppler spectrum of point B in Figure 11b; Blue solid and red dashed lines are the measured and modeled Doppler spectra, respectively.

The centroids of the Doppler spectra depicted in Figure 12a,b have been shifted to zero. The blue solid lines are the measured Doppler spectra that is calculated directly from the single-look complex image, and the red dashed lines are the Doppler spectra modeled by Equation (5), in which $\overline{\sigma}(x_0, y_0)$, $\overline{\sigma}(x_0 + D_x, y_0 + D_y)$, $\overline{\sigma}(x_0 - D_x, y_0 - D_y)$, $P_a(f)$, and N_0 are all known from the raw data. Point A is an uncontaminated target, so its Doppler spectrum satisfies a typical Gaussian function quite well (Figure 12a). The accordance between the measured and modeled spectra validates the accuracy of the proposed method. As a comparison, point B is a target seriously contaminated by the azimuthal ambiguity effect. The low-frequency and high-frequency parts of the Doppler spectrum of B (Figure 12b) are very high; they correspond to the ambiguity signals from the right and left sides of point B, respectively. The spectrum at low frequency is especially high. From Figure 11a, it is known that the left and right sides of point B are all high-backscattering land targets, whereas point B is a water area with a very low NRCS, and the target on the right is much stronger than on the left. The NRCS distribution of Figure 11a agrees with the analysis of the Doppler spectrum of point B

and the modeled spectrum satisfies the measured spectrum quite well, which further validates the proposed method.

4. Discussion

As SAR imaging is more and more widely used, the radar echo is analyzed in the proposed method, and the relative value of RCS is extracted from the Doppler spectrum, the estimated relative backscattering intensity is converted to absolute NRCS using Equation (27). The comparison between the proposed method and the traditional method is described in detail in Section 3. Three examples show the feasibility and superiority of the proposed method. In the following, the estimation accuracy of the proposed method and the traditional method is analyzed by simulation.

Because the normalized image intensity differs from the NRCS only with a constant offset, the proposed method uses the normalized image intensity to be equivalent to NRCS. In this paper, in order to simplify the calculation without the loss of equivalence, the normalized image intensity is adopted in Figures 6, 8 and 9.

The Comparative Simulation Analysis of Estimation Accuracy for Different NRCS Estimation Methods

The simulations were performed under different signal-to-noise ratios (SNR) and azimuthal ambiguity conditions. The parameters of the simulations are given in Table 2, which correspond to low, intermediate, and high azimuthal ambiguity, respectively.

Table 2. Simulation parameters.

	Simulation 1	**Simulation 2**	**Simulation 3**
$\overline{\sigma}(x_0, y_0)/N_0$	0.01–0.5	0.01–0.5	0.01–0.5
$\overline{\sigma}(x_0 - D_x, y_0 - D_y)/N_0$, $\overline{\sigma}(x_0 + D_x, y_0 + D_y)/N_0$	2	5	10
Simulation repeat number	400	400	400
Pixel number used for calculating one Doppler spectrum	80	80	80

Take the estimation precision of ML estimation into consideration; according to mathematical statistics theory, the ML estimation can reach the Cramer–Rao bound [12,13]. That is the root-mean-square (rms) of the estimation which can be expressed as:

$$rms[\hat{\sigma}_n] = \frac{1}{\sqrt{-E\left[\frac{\partial^2 \ln g\left(\begin{array}{cccccc} p_{n-X} & p_n & p_{n+X} & I_n & \end{array}\middle| \overline{\sigma}_n\right)}{\partial \overline{\sigma}_n^2}\right]}} = \frac{1}{\sqrt{\begin{array}{c}\sum\limits_{i=1}^{m} \frac{P_C^2(f_i)}{\left[\overline{\sigma}_{n-X} P_L(f_i) + \overline{\sigma}_n P_C(f_i) + \overline{\sigma}_{n+X} P_R(f_i) + \frac{N_0}{F_r}\right]^2} + \sum\limits_{i=1}^{m} \frac{P_R^2(f_i)}{\left[\overline{\sigma}_{n-2X} P_L(f_i) + \overline{\sigma}_{n-X} P_C(f_i) + \overline{\sigma}_n P_R(f_i) + \frac{N_0}{F_r}\right]^2} \\ + \sum\limits_{i=1}^{m} \frac{P_L^2(f_i)}{\left[\overline{\sigma}_n P_L(f_i) + \overline{\sigma}_{n+X} P_C(f_i) + \overline{\sigma}_{n+2X} P_R(f_i) + \frac{N_0}{F_r}\right]^2} + \frac{N}{\overline{\sigma}_n^2}\end{array}}} \quad (28)$$

where $\hat{\sigma}(x_0, y_0)$ is the ML estimation of $\overline{\sigma}(x_0, y_0)$, and $rms[\bullet]$ refers to the root–mean–square.

The rms of the modified method is shown in Figure 13. For comparison, the Cramer–Rao bound of ML estimation and the simple estimation of $I - N_0$, which is used in Equation (1), are also depicted in Figure 13.

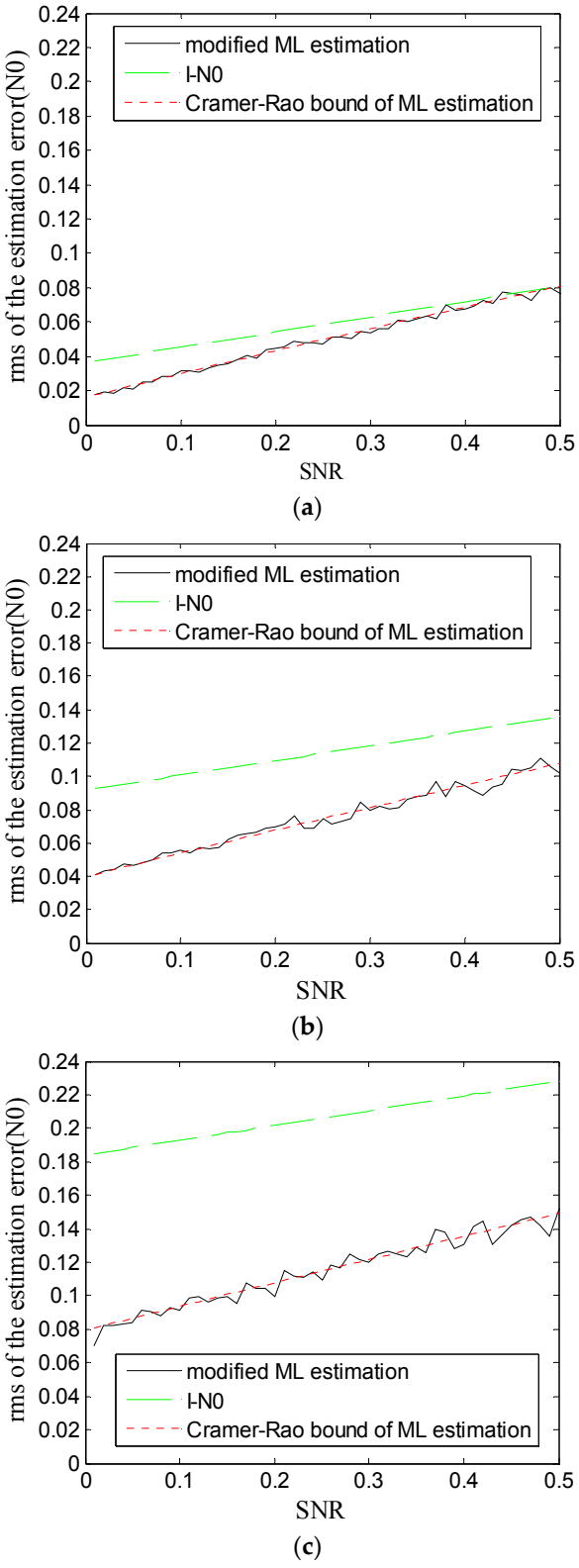

Figure 13. The comparison of three kinds of estimation precision, rms of estimation error of modified estimation method (black solid line), $I - N_0$ (green dashed line), and Cramer–Rao bound of maximum likelihood (ML) estimation (red dotted line), (**a**) for simulation 1; (**b**) for simulation 2; and (**c**) for simulation 3.

In Figure 13, the SNR (x-axis) refers to $\overline{\sigma}(x_0, y_0)/N_0$, and the estimation error (y-axis) is normalized by N_0. A comparison of Figure 13a, Figure 13b, and Figure 13c clearly shows that the estimation error of the simple estimation $I - N_0$ increases significantly with increasing azimuthal ambiguity, but the results from the proposed method of estimation can almost maintain the same estimation precision under various azimuthal ambiguity conditions. Even under low azimuthal ambiguity conditions (Figure 13a), the estimation error of the proposed estimation method is also significantly less than that of simple estimation $I - N_0$. In Figure 13a–c, it indicates that the rms of the estimation error of the proposed estimation method is very close to the Cramer–Rao bound with the increase in SNR. This result validates that the proposed estimation method can significantly increase estimation precision under a low SNR or low-scattering area in SAR images.

Take the low SNR condition into account, supposing $\overline{\sigma}(x_0, y_0) << N_0$; neglecting the contribution from the azimuthal ambiguity effect, the rms of the estimation error of the proposed estimation method can be obtained as:

$$rms[\hat{\sigma}(x_0, y_0)] \approx 0.8 \frac{N_0}{F_r \sqrt{\sum_{i=1}^{m} P_a^2(f_i - f_0)}} \tag{29}$$

The Doppler power spectrum can often be obtained by incoherently averaging the spectra of several uncorrelated signals. The estimation precision derived so far is also applicable in the case when the number m is replaced by the overall number of pixels contributing to the estimation.

For example, assume that the NESZ of a spaceborne SAR is -25 dB, the single-look pixel size is 8 m (look direction) $\times$ 5 m (flight direction), and the number of pixels contributing to one estimation is 240 (in each estimation, the Doppler spectrum is calculated from 20 pixels in the flight direction and incoherently averaged by 12 times in the look direction); an NRCS estimation precision of about -38 dB could be acquired in the low-backscattering area at a resolution of 96 m $\times$ 100 m.

5. Conclusions

The image intensities of SAR images of low-backscattering areas are often affected by the system noise and azimuthal ambiguity effect. In this paper, a method is proposed for estimating the NRCS of low-backscattering areas. The method can eliminate much of the effect of system noise and azimuthal ambiguity. This method is based on the single-look complex image, and the azimuthal matching filter in the imaging algorithm must be an unweighted filter. The parameters needed for this method can all be estimated from the single-look complex image itself, which makes the method easy to apply. An analysis on the estimation precision demonstrates that, for a typical spaceborne SAR with a NESZ of -25 dB and a single-look pixel size of 8 m $\times$ 5 m, the NRCS estimation precision of low-backscattering areas can reach -38 dB at a resolution of 96 m $\times$ 100 m.

Three examples are given for validation in Section 3. The first example is a SAR image that is an oceanic internal wave. In the conventional SAR image, the troughs of the internal wave signal intensity are buried by the noise floor, making it hard to judge the exact trough position. In contrast, the NRCS estimated by the proposed method can recover the texture features of the low-scattering area much better, and the recovered troughs of the internal wave are located near the midpoint of the adjacent peaks. The result is a qualitative analysis for the estimation method in low NRCS. In addition, the example in Section 3.2 is atmospheric gravity waves. The estimation values of signal intensity by the proposed method in this paper are very close to the theoretical value of the signal intensity in the low-scattering area of the original image. The result is a quantitative analysis for the estimation method in low NRCS. The third example is a SAR image of a land-water junction, in which the water area is seriously affected by the azimuthal ambiguity signals from high-backscattering land targets. As a comparison, the azimuthal ambiguity signals are filtered out quite clearly in the NRCS image estimated by the proposed method. The Doppler spectra of two points were analyzed, one contaminated and one uncontaminated by the azimuthal ambiguity signal. Analysis proves that the Doppler spectra modeled by the proposed method can satisfy the actual Doppler spectra calculated from the single-look complex

image quite well. These three examples both indirectly and directly validate the feasibility of the proposed method in this paper.

This proposed method can be applied to SAR image processing in low-scattering areas in the ocean, such as internal waves, oil spills, low wind speed zones, upwelling, and so on. Conversely, the proposed method can be applied to the data processing of the SAR satellite system with lower NESZ, which can reduce the cost of satellites and improve the bandwidth, resolution, and other indicators of the SAR system.

Acknowledgments: This work was supported by the National Natural Science Foundation of China (No. 41276185).

Author Contributions: Hui Meng and Xiaoqing Wang conceived and performed the experiments; Xiaoqing Wang and Jinsong Chong supervised and designed the research and contributed to the article's organization; Xiangfei Wei and Weiya Kong provided the data for comparative analysis. Hui Meng and Xiaoqing Wang drafted the manuscript, which was revised by all authors. All authors read and approved the final manuscript.

Conflicts of Interest: The authors declare no conflict of interest.

Appendix A. The Jacobian Matrix of the Derived Function

When $2X < n \leq \mathrm{T} - 2X$

$$
\begin{aligned}
J(n,n-2X) &= \sum_{i=1}^{m} \frac{P_L(f_i)P_R(f_i)}{\left[\overline{\sigma}_n P_L(f_i) + \overline{\sigma}_{n+X} P_C(f_i) + \overline{\sigma}_{n+2X} P_R(f_i) + \frac{N_0}{F_r}\right]^2} - 2\sum_{i=1}^{m} \frac{p_{n-X}(f_i)P_L(f_i)P_R(f_i)}{\left[\overline{\sigma}_{n-2X} P_L(f_i) + \overline{\sigma}_{n-X} P_C(f_i) + \overline{\sigma}_n P_R(f_i) + \frac{N_0}{F_r}\right]^3} \\
J(n,n-X) = J(n,n) &= \sum_{i=1}^{m} \frac{P_C(f_i)P_L(f_i)}{\left[\overline{\sigma}_{n-X} P_L(f_i) + \overline{\sigma}_n P_C(f_i) + \overline{\sigma}_{n+X} P_R(f_i) + \frac{N_0}{F_r}\right]^2} + \sum_{i=1}^{m} \frac{P_C(f_i)P_R(f_i)}{\left[\overline{\sigma}_{n-2X} P_L(f_i) + \overline{\sigma}_{n-X} P_C(f_i) + \overline{\sigma}_n P_R(f_i) + \frac{N_0}{F_r}\right]^2} \\
&-2\sum_{i=1}^{m} \frac{p_n(f_i)P_C(f_i)P_L(f_i)}{\left[\overline{\sigma}_{n-X} P_L(f_i) + \overline{\sigma}_n P_C(f_i) + \overline{\sigma}_{n+X} P_R(f_i) + \frac{N_0}{F_r}\right]^3} - 2\sum_{i=1}^{m} \frac{p_{n-X}(f_i)P_C(f_i)P_R(f_i)}{\left[\overline{\sigma}_{n-2X} P_L(f_i) + \overline{\sigma}_{n-X} P_C(f_i) + \overline{\sigma}_n P_R(f_i) + \frac{N_0}{F_r}\right]^3} \\
J(n,n) &= \sum_{i=1}^{m} \frac{P_C^2(f_i)}{\left[\overline{\sigma}_{n-X} P_L(f_i) + \overline{\sigma}_n P_C(f_i) + \overline{\sigma}_{n+X} P_R(f_i) + \frac{N_0}{F_r}\right]^2} + \sum_{i=1}^{m} \frac{P_R^2(f_i)}{\left[\overline{\sigma}_{n-2X} P_L(f_i) + \overline{\sigma}_{n-X} P_C(f_i) + \overline{\sigma}_n P_R(f_i) + \frac{N_0}{F_r}\right]^2} \\
&+\sum_{i=1}^{m} \frac{P_L^2(f_i)}{\left[\overline{\sigma}_n P_L(f_i) + \overline{\sigma}_{n+X} P_C(f_i) + \overline{\sigma}_{n+2X} P_R(f_i) + \frac{N_0}{F_r}\right]^2} - 2\sum_{i=1}^{m} \frac{p_n(f_i)P_C^2(f_i)}{\left[\overline{\sigma}_{n-X} P_L(f_i) + \overline{\sigma}_n P_C(f_i) + \overline{\sigma}_{n+X} P_R(f_i) + \frac{N_0}{F_r}\right]^3} \\
&-2\sum_{i=1}^{m} \frac{p_{n-X}(f_i)P_R^2(f_i)}{\left[\overline{\sigma}_{n-2X} P_L(f_i) + \overline{\sigma}_{n-X} P_C(f_i) + \overline{\sigma}_n P_R(f_i) + \frac{N_0}{F_r}\right]^3} - 2\sum_{i=1}^{m} \frac{p_{n+X}(f_i)P_L^2(f_i)}{\left[\overline{\sigma}_n P_L(f_i) + \overline{\sigma}_{n+X} P_C(f_i) + \overline{\sigma}_{n+2X} P_R(f_i) + \frac{N_0}{F_r}\right]^3} \\
&-\left[\frac{\alpha^2[2\alpha\overline{\sigma}_n(\frac{\pi}{2} + \arctan(\alpha\overline{\sigma}_n)) + 1]}{[1 + (\alpha\overline{\sigma}_n)^2]^2[\frac{\pi}{2} + \arctan(\alpha\overline{\sigma}_n)]^2}\right] \\
J(n,n+X) &= \sum_{i=1}^{m} \frac{P_C(f_i)P_R(f_i)}{\left[\overline{\sigma}_{n-X} P_L(f_i) + \overline{\sigma}_n P_C(f_i) + \overline{\sigma}_{n+X} P_R(f_i) + \frac{N_0}{F_r}\right]^2} + \sum_{i=1}^{m} \frac{P_C(f_i)P_L(f_i)}{\left[\overline{\sigma}_n P_L(f_i) + \overline{\sigma}_{n+X} P_C(f_i) + \overline{\sigma}_{n+2X} P_R(f_i) + \frac{N_0}{F_r}\right]^2} \\
&-2\sum_{i=1}^{m} \frac{p_n(f_i)P_C(f_i)P_R(f_i)}{\left[\overline{\sigma}_{n-X} P_L(f_i) + \overline{\sigma}_n P_C(f_i) + \overline{\sigma}_{n+X} P_R(f_i) + \frac{N_0}{F_r}\right]^3} - 2\sum_{i=1}^{m} \frac{p_{n+X}(f_i)P_C(f_i)P_L(f_i)}{\left[\overline{\sigma}_n P_L(f_i) + \overline{\sigma}_{n+X} P_C(f_i) + \overline{\sigma}_{n+2X} P_R(f_i) + \frac{N_0}{F_r}\right]^3} \\
J(n,n+2X) &= \sum_{i=1}^{m} \frac{P_R(f_i)P_L(f_i)}{\left[\overline{\sigma}_n P_L(f_i) + \overline{\sigma}_{n+X} P_C(f_i) + \overline{\sigma}_{n+2X} P_R(f_i) + \frac{N_0}{F_r}\right]^2} - 2\sum_{i=1}^{m} \frac{p_{n+X}(f_i)P_R(f_i)P_L(f_i)}{\left[\overline{\sigma}_n P_L(f_i) + \overline{\sigma}_{n+X} P_C(f_i) + \overline{\sigma}_{n+2X} P_R(f_i) + \frac{N_0}{F_r}\right]^3}
\end{aligned}
\tag{A1}
$$

When $X < n \leq 2X$

$$
\begin{aligned}
J(n,n-X) &= \sum_{i=1}^{m} \frac{P_C(f_i)P_L(f_i)}{\left[\overline{\sigma}_{n-X}P_L(f_i)+\overline{\sigma}_n P_C(f_i)+\overline{\sigma}_{n+X}P_R(f_i)+\frac{N_0}{F_r}\right]^2} + \sum_{i=1}^{m} \frac{P_L^2(f_i)}{\left[\overline{\sigma}_n P_L(f_i)+\overline{\sigma}_{n+X}P_C(f_i)+\overline{\sigma}_{n+2X}P_R(f_i)+\frac{N_0}{F_r}\right]^2} \\
&-2\sum_{i=1}^{m} \frac{p_n(f_i)P_C^2(f_i)}{\left[\overline{\sigma}_{n-X}P_L(f_i)+\overline{\sigma}_n P_C(f_i)+\overline{\sigma}_{n+X}P_R(f_i)+\frac{N_0}{F_r}\right]^3} - 2\sum_{i=1}^{m} \frac{p_{n+X}(f_i)P_L^2(f_i)}{\left[\overline{\sigma}_n P_L(f_i)+\overline{\sigma}_{n+X}P_C(f_i)+\overline{\sigma}_{n+2X}P_R(f_i)+\frac{N_0}{F_r}\right]^3} \\
J(n,n) &= \sum_{i=1}^{m} \frac{P_C^2(f_i)}{\left[\overline{\sigma}_{n-X}P_L(f_i)+\overline{\sigma}_n P_C(f_i)+\overline{\sigma}_{n+X}P_R(f_i)+\frac{N_0}{F_r}\right]^2} + \sum_{i=1}^{m} \frac{P_L^2(f_i)}{\left[\overline{\sigma}_n P_L(f_i)+\overline{\sigma}_{n+X}P_C(f_i)+\overline{\sigma}_{n+2X}P_R(f_i)+\frac{N_0}{F_r}\right]^2} \\
&-2\sum_{i=1}^{m} \frac{p_n(f_i)P_C^2(f_i)}{\left[\overline{\sigma}_{n-X}P_L(f_i)+\overline{\sigma}_n P_C(f_i)+\overline{\sigma}_{n+X}P_R(f_i)+\frac{N_0}{F_r}\right]^3} - 2\sum_{i=1}^{m} \frac{p_{n+X}(f_i)P_L^2(f_i)}{\left[\overline{\sigma}_n P_L(f_i)+\overline{\sigma}_{n+X}P_C(f_i)+\overline{\sigma}_{n+2X}P_R(f_i)+\frac{N_0}{F_r}\right]^3} \\
&-\left[\frac{\alpha^2[2\alpha\overline{\sigma}_n(\frac{\pi}{2}+\arctan(\alpha\overline{\sigma}_n))+1]}{[1+(\alpha\overline{\sigma}_n)^2]^2[\frac{\pi}{2}+\arctan(\alpha\overline{\sigma}_n)]^2}\right] \\
J(n,n+X) &= \sum_{i=1}^{m} \frac{P_C(f_i)P_R(f_i)}{\left[\overline{\sigma}_{n-X}P_L(f_i)+\overline{\sigma}_n P_C(f_i)+\overline{\sigma}_{n+X}P_R(f_i)+\frac{N_0}{F_r}\right]^2} + \sum_{i=1}^{m} \frac{P_C(f_i)P_L(f_i)}{\left[\overline{\sigma}_n P_L(f_i)+\overline{\sigma}_{n+X}P_C(f_i)+\overline{\sigma}_{n+2X}P_R(f_i)+\frac{N_0}{F_r}\right]^2} \\
&-2\sum_{i=1}^{m} \frac{p_n(f_i)P_C(f_i)P_R(f_i)}{\left[\overline{\sigma}_{n-X}P_L(f_i)+\overline{\sigma}_n P_C(f_i)+\overline{\sigma}_{n+X}P_R(f_i)+\frac{N_0}{F_r}\right]^3} - 2\sum_{i=1}^{m} \frac{p_{n+X}(f_i)P_C(f_i)P_L(f_i)}{\left[\overline{\sigma}_n P_L(f_i)+\overline{\sigma}_{n+X}P_C(f_i)+\overline{\sigma}_{n+2X}P_R(f_i)+\frac{N_0}{F_r}\right]^3} \\
J(n,n+2X) &= \sum_{i=1}^{m} \frac{P_L(f_i)P_R(f_i)}{\left[\overline{\sigma}_n P_L(f_i)+\overline{\sigma}_{n+X}P_C(f_i)+\overline{\sigma}_{n+2X}P_R(f_i)+\frac{N_0}{F_r}\right]^2} - 2\sum_{i=1}^{m} \frac{p_{n+X}(f_i)P_L(f_i)P_R(f_i)}{\left[\overline{\sigma}_n P_L(f_i)+\overline{\sigma}_{n+X}P_C(f_i)+\overline{\sigma}_{n+2X}P_R(f_i)+\frac{N_0}{F_r}\right]^3}
\end{aligned}
\tag{A2}
$$

When $0 < n \leq X$

$$
\begin{aligned}
J(n,n) &= \sum_{i=1}^{m} \frac{P_L^2(f_i)}{\left[\overline{\sigma}_n P_L(f_i)+\overline{\sigma}_{n+X}P_C(f_i)+\overline{\sigma}_{n+2X}P_R(f_i)+\frac{N_0}{F_r}\right]^2} - 2\sum_{i=1}^{m} \frac{p_{n+X}(f_i)P_L^2(f_i)}{\left[\overline{\sigma}_n P_L(f_i)+\overline{\sigma}_{n+X}P_C(f_i)+\overline{\sigma}_{n+2X}P_R(f_i)+\frac{N_0}{F_r}\right]^3} \\
&-\left[\frac{\alpha^2[2\alpha\overline{\sigma}_n(\frac{\pi}{2}+\arctan(\alpha\overline{\sigma}_n))+1]}{[1+(\alpha\overline{\sigma}_n)^2]^2[\frac{\pi}{2}+\arctan(\alpha\overline{\sigma}_n)]^2}\right] \\
J(n,n+X) &= \sum_{i=1}^{m} \frac{P_L(f_i)P_C(f_i)}{\left[\overline{\sigma}_n P_L(f_i)+\overline{\sigma}_{n+X}P_C(f_i)+\overline{\sigma}_{n+2X}P_R(f_i)+\frac{N_0}{F_r}\right]^2} - 2\sum_{i=1}^{m} \frac{p_{n+X}(f_i)P_L(f_i)P_C(f_i)}{\left[\overline{\sigma}_n P_L(f_i)+\overline{\sigma}_{n+X}P_C(f_i)+\overline{\sigma}_{n+2X}P_R(f_i)+\frac{N_0}{F_r}\right]^3} \\
J(n,n+2X) &= \sum_{i=1}^{m} \frac{P_L(f_i)P_R(f_i)}{\left[\overline{\sigma}_n P_L(f_i)+\overline{\sigma}_{n+X}P_C(f_i)+\overline{\sigma}_{n+2X}P_R(f_i)+\frac{N_0}{F_r}\right]^2} - 2\sum_{i=1}^{m} \frac{p_{n+X}(f_i)P_L(f_i)P_R(f_i)}{\left[\overline{\sigma}_n P_L(f_i)+\overline{\sigma}_{n+X}P_C(f_i)+\overline{\sigma}_{n+2X}P_R(f_i)+\frac{N_0}{F_r}\right]^3}
\end{aligned}
\tag{A3}
$$

When $\mathrm{T} - 2X < n \leq \mathrm{T} - X$

$$
\begin{aligned}
J(n,n-2X) &= \sum_{i=1}^{m} \frac{P_L(f_i)P_R(f_i)}{\left[\overline{\sigma}_{n-2X}P_L(f_i)+\overline{\sigma}_{n-X}P_C(f_i)+\overline{\sigma}_n P_R(f_i)+\frac{N_0}{F_r}\right]^2} - 2\sum_{i=1}^{m} \frac{p_{n-X}(f_i)P_L(f_i)P_R(f_i)}{\left[\overline{\sigma}_{n-2X}P_L(f_i)+\overline{\sigma}_{n-X}P_C(f_i)+\overline{\sigma}_n P_R(f_i)+\frac{N_0}{F_r}\right]^3} \\
J(n,n) &= \sum_{i=1}^{m} \frac{P_C^2(f_i)}{\left[\overline{\sigma}_{n-X}P_L(f_i)+\overline{\sigma}_n P_C(f_i)+\overline{\sigma}_{n+X}P_R(f_i)+\frac{N_0}{F_r}\right]^2} + \sum_{i=1}^{m} \frac{P_R^2(f_i)}{\left[\overline{\sigma}_{n-2X}P_L(f_i)+\overline{\sigma}_{n-X}P_C(f_i)+\overline{\sigma}_n P_R(f_i)+\frac{N_0}{F_r}\right]^2} \\
&-2\sum_{i=1}^{m} \frac{p_n(f_i)P_C^2(f_i)}{\left[\overline{\sigma}_{n-X}P_L(f_i)+\overline{\sigma}_n P_C(f_i)+\overline{\sigma}_{n+X}P_R(f_i)+\frac{N_0}{F_r}\right]^3} - 2\sum_{i=1}^{m} \frac{p_{n-X}(f_i)P_R^2(f_i)}{\left[\overline{\sigma}_{n-2X}P_L(f_i)+\overline{\sigma}_{n-X}P_C(f_i)+\overline{\sigma}_n P_R(f_i)+\frac{N_0}{F_r}\right]^3} \\
&-\left[\frac{\alpha^2[2\alpha\overline{\sigma}_n(\frac{\pi}{2}+\arctan(\alpha\overline{\sigma}_n))+1]}{[1+(\alpha\overline{\sigma}_n)^2]^2[\frac{\pi}{2}+\arctan(\alpha\overline{\sigma}_n)]^2}\right] \\
J(n,n+X) &= \sum_{i=1}^{m} \frac{P_C(f_i)P_R(f_i)}{\left[\overline{\sigma}_{n-X}P_L(f_i)+\overline{\sigma}_n P_C(f_i)+\overline{\sigma}_{n+X}P_R(f_i)+\frac{N_0}{F_r}\right]^2} - 2\sum_{i=1}^{m} \frac{p_n(f_i)P_C(f_i)P_R(f_i)}{\left[\overline{\sigma}_{n-X}P_L(f_i)+\overline{\sigma}_n P_C(f_i)+\overline{\sigma}_{n+X}P_R(f_i)+\frac{N_0}{F_r}\right]^3}
\end{aligned}
\tag{A4}
$$

When $T - X < n \leq T$

$$
\begin{aligned}
J(n, n-2X) &= \sum_{i=1}^{m} \frac{P_L(f_i)P_R(f_i)}{\left[\overline{\sigma}_{n-2X}P_L(f_i) + \overline{\sigma}_{n-X}P_C(f_i) + \overline{\sigma}_n P_R(f_i) + \frac{N_0}{F_r}\right]^2} - 2\sum_{i=1}^{m} \frac{p_{n-X}(f_i)P_L(f_i)P_R(f_i)}{\left[\overline{\sigma}_{n-2X}P_L(f_i) + \overline{\sigma}_{n-X}P_C(f_i) + \overline{\sigma}_n P_R(f_i) + \frac{N_0}{F_r}\right]^3} \\
J(n, n-X) &= \sum_{i=1}^{m} \frac{P_C(f_i)P_R(f_i)}{\left[\overline{\sigma}_{n-2X}P_L(f_i) + \overline{\sigma}_{n-X}P_C(f_i) + \overline{\sigma}_n P_R(f_i) + \frac{N_0}{F_r}\right]^2} - 2\sum_{i=1}^{m} \frac{p_{n-X}(f_i)P_C(f_i)P_R(f_i)}{\left[\overline{\sigma}_{n-2X}P_L(f_i) + \overline{\sigma}_{n-X}P_C(f_i) + \overline{\sigma}_n P_R(f_i) + \frac{N_0}{F_r}\right]^3} \\
J(n, n) &= \sum_{i=1}^{m} \frac{P_R^2(f_i)}{\left[\overline{\sigma}_{n-2X}P_L(f_i) + \overline{\sigma}_{n-X}P_C(f_i) + \overline{\sigma}_n P_R(f_i) + \frac{N_0}{F_r}\right]^2} - 2\sum_{i=1}^{m} \frac{p_{n-X}(f_i)P_R^2(f_i)}{\left[\overline{\sigma}_{n-2X}P_L(f_i) + \overline{\sigma}_{n-X}P_C(f_i) + \overline{\sigma}_n P_R(f_i) + \frac{N_0}{F_r}\right]^3} \\
&- \left[\frac{\alpha^2[2\alpha\overline{\sigma}_n(\frac{\pi}{2} + \arctan(\alpha\overline{\sigma}_n)) + 1]}{[1 + (\alpha\overline{\sigma}_n)^2]^2[\frac{\pi}{2} + \arctan(\alpha\overline{\sigma}_n)]^2}\right]
\end{aligned}
\tag{A5}
$$

References

1. Kerbaol, V.; Collard, F. SAR-derived coastal and marine applications: From research to operational products. *IEEE J. Ocean. Eng.* **2005**, *30*, 472–486. [CrossRef]
2. Solberg, A.S.; Storvik, G.; Solberg, R.; Volden, E. Automatic detection of oil spills in ERS SAR images. *IEEE Trans. Geosci. Remote Sens.* **1999**, *37*, 1916–1924. [CrossRef]
3. Wei, Z. *Synthetic Aperture Radar Satellite*; Sciences Press: Beijing, China, 2001. (In Chinese)
4. Massonnet, D.; Souyris, J.-C. *Imaging with Synthetic Aperture Radar*; CRC Press: Boca Raton, FL, USA, 2008.
5. Lukowski, T.; St-Jean, R.; Hawkins, R.; Draper, K.; Hamm, P.; Teany, L. Ers-1 SAR Calibration Studies: Preparation for Radarsat. In Proceedings of the International Geoscience and Remote Sensing Symposium, Better Understanding of Earth Environment, Tokyo, Japan, 18–21 August 1993.
6. Lukowski, T.; Hawkins, R.; Moucha, R.; Khandelwal, T.; Neeson, I. Spaceborne SAR calibration studies: Ers-1. In Proceedings of the International Geoscience and Remote Sensing Symposium, Surface and Atmospheric Remote Sensing: Technologies, Data Analysis and Interpretation, Pasadena, CA, USA, 8–12 August 1994.
7. Rosich, B.; Meadows, P. *Absolute Calibration of ASAR Level 1 Products Generated with PF-ASAR*; ESA Document; European Space Agency: Frascati, Italy, 2004.
8. Laur, H.; Bally, P.; Meadows, P.; Sánchez, J.; Schättler, B.; Lopinto, E.; Esteban, D. *ERS SAR Calibration: Derivation of σ0 in ESA ERS SAR PRI Products*; ESA/ESRIN, ES-TN-RS-PM-HL09; European Space Agency/ESRIN: Frascati, Italy, 2003.
9. Lavalle, M.; Wright, T. *Absolute Radiometric and Polarimetric Calibration of Alos Palsar Products*; European Space Agency: Paris, France, 2009.
10. RADARSAT International. *Radarsat-1 Data Product Specification*; RADARSAT International: Richmond, BC, Canada, 2004.
11. Cumming, I.G.; Wong, F.H. *Digital Processing of Synthetic Aperture Radar Data*; Artech House: London, UK, 2005.
12. Zhang, X. *Modern Signal Processing*; Tsinghua University Press: Beijing, China, 2002. (In Chinese)
13. Sage, A.P.; Melsa, J.L. *Estimation Theory with Applications to Communications and Control*; DTIC Document; McGraw-Hill Book Co.: New York, NY, USA, 1971.
14. Gao, G. Statistical modeling of SAR images: A survey. *Sensors* **2010**, *10*, 775–795. [CrossRef] [PubMed]
15. Bamler, R. Doppler frequency estimation and the cramer-rao bound. *IEEE Trans. Geosci. Remote Sens.* **1991**, *29*, 385–390. [CrossRef]
16. Madsen, S.N. Estimating the Doppler centroid of SAR data. *IEEE Trans. Aerosp. Electron. Syst.* **1989**, *25*, 134–140. [CrossRef]
17. Bamler, R.; Runge, H. Prf-ambiguity resolving by wavelength diversity. *IEEE Trans. Geosci. Remote Sens.* **1991**, *29*, 997–1003. [CrossRef]
18. Wong, F.; Cumming, I.G. A combined SAR Doppler centroid estimation scheme based upon signal phase. *IEEE Trans. Geosci. Remote Sens.* **1996**, *34*, 696–707. [CrossRef]
19. Chang, C.-Y.; Curlander, J.C. Application of the multiple PRF technique to resolve Doppler centroid estimation ambiguity for spaceborne SAR. *IEEE Trans. Geosci. Remote Sens.* **1992**, *30*, 941–949. [CrossRef]

20. Chapron, B.; Collard, F.; Ardhuin, F. Direct measurements of ocean surface velocity from space: Interpretation and validation. *J. Geophys. Res. Oceans* **2005**, *110*, 691–706. [CrossRef]
21. Hansen, M.W.; Collard, F.; Dagestad, K.; Johannessen, J.A.; Fabry, P.; Chapron, B. Retrieval of sea surface range velocities from envisat asar doppler centroid measurements. *IEEE Trans. Geosci. Remote Sens.* **2011**, *49*, 3582–3592. [CrossRef]
22. Johannessen, J.A.; Chapron, B.; Collard, F.; Kudryavtsev, V.; Mouche, A.; Akimov, D.; Dagestad, K.F. Direct ocean surface velocity measurements from space: Improved quantitative interpretation of ENVISAT ASAR observations. *Geophys. Res. Lett.* **2008**, *35*, 113–130. [CrossRef]
23. Wang, P.; Wang, X.; Chong, J.; Lu, Y. Optimal parameter estimation method of internal solitary waves in SAR images and the Cramér–Rao bound. *IEEE Trans. Geosci. Remote Sens.* **2016**, *54*, 3143–3150. [CrossRef]